

Materials Horizons

Accepted Manuscript

This article can be cited before page numbers have been issued, to do this please use: A. Landi, F. Ambrosio, N. Bianchi, M. Loriso, L. Malvasi, A. Profumo, J. Wiktor and A. Peluso, *Mater. Horiz.*, 2026, DOI: 10.1039/D6MH00462H.



This is an Accepted Manuscript, which has been through the Royal Society of Chemistry peer review process and has been accepted for publication.

Accepted Manuscripts are published online shortly after acceptance, before technical editing, formatting and proof reading. Using this free service, authors can make their results available to the community, in citable form, before we publish the edited article. We will replace this Accepted Manuscript with the edited and formatted Advance Article as soon as it is available.

You can find more information about Accepted Manuscripts in the [Information for Authors](#).

Please note that technical editing may introduce minor changes to the text and/or graphics, which may alter content. The journal's standard [Terms & Conditions](#) and the [Ethical guidelines](#) still apply. In no event shall the Royal Society of Chemistry be held responsible for any errors or omissions in this Accepted Manuscript or any consequences arising from the use of any information it contains.

New Concepts

Defect engineering has emerged as a cornerstone strategy for tuning the photocatalytic performance of graphitic carbon nitride (g-C₃N₄), yet the field has long lacked a unified microscopic picture connecting atomic-scale vacancy structures to measurable device-level outcomes. The prevailing approach - modelling defects in small, idealized flat supercells - misses a physically crucial ingredient: the long-range, collective out-of-plane buckling that is intrinsic to this two-dimensional material. This work introduces the concept that structural corrugation is not a minor geometric detail but a thermodynamic determinant of which nitrogen vacancy actually forms and dominates in real samples. By deploying hybrid density functional theory on supercells exceeding one thousand atoms, we demonstrate that neglecting long-range buckling can even invert the predicted stability ordering of competing defect configurations - a qualitative error with direct consequences for interpreting experiments. Beyond structural insights, the framework establishes, for the first time, a quantitative and self-consistent link between defect-induced electronic levels and three distinct classes of experimental observable: red-shifted optical absorption, photoluminescence quenching, and the asymmetric enhancement of photo-reduction versus suppression of photo-oxidation activity. This "defect-to-function" predictive protocol is transferable to other two-dimensional carbon nitrides and metal-free photocatalysts, offering the materials community a rigorous computational blueprint for rationally engineering defective semiconductors with precisely tailored optoelectronic and catalytic selectivity.



Data availability statement

View Article Online
DOI: 10.1039/D6MH00462H

The data supporting this article have been included as part of the Supplementary Information.



Cite this: DOI: 00.0000/xxxxxxxxxx

Nitrogen Vacancies in Graphitic Carbon Nitride and their Role in Heterogeneous Photocatalysis[†]

Alessandro Landi,^{*a} Francesco Ambrosio,^{*b} Nadia Bianchi,^a Michele Loriso,^b Lorenzo Malavasi,^c Antonella Profumo,^d Julia Wiktor,^e and Andrea Peluso,^{*a}Received Date
Accepted Date

DOI: 00.0000/xxxxxxxxxx

Graphitic carbon nitride (g-C₃N₄) is a promising metal-free photocatalyst whose activity is often enhanced by nitrogen vacancies, though their microscopic role remains unclear. Using advanced ab initio calculations with large periodic supercells, we show that long-range buckling is essential to correctly evaluate defect energetics and thus determine the stability of distinct vacancy configurations. The most stable defects are found to introduce localized in-gap states corresponding to shallow acceptor and deep donor levels. These features explain (i) the experimental red-shifted absorption and (ii) suppressed photoluminescence observed in N-deficient g-C₃N₄ samples. Most importantly (iii) energy-level alignment at the water-semiconductor interface explains the enhanced photocatalytic reduction and reduced oxidation activity reported experimentally. Overall, our results provide a unified microscopic picture that quantitatively connects defect-induced electronic structure changes and experimental observables, offering concrete predictive strategy for designing defect engineered carbon nitride and related metal-free photocatalysts.

Keywords: Graphitic carbon nitride; Nitrogen vacancies; Defect engineering; Photocatalysis; Metal-free photocatalysts; Long-range

buckling; Structure-property relationships

Introduction

Graphitic carbon nitride (g-C₃N₄) is a metal-free semiconductor with remarkable potential for sustainable technologies.^{1–3} It is constituted by fused heptazine (tri-s-triazine) units (see Figure 1) and can be synthesized cheaply by thermal condensation of nitrogen-rich precursors (e.g. melamine or urea)^{4,5}. This facile, low-cost preparation yields a chemically and thermally stable layered network, that exhibits a moderate band gap (≈ 2.7 – 2.8 eV) enabling visible-light absorption. These properties – together with a tunable electronic structure – make g-C₃N₄ attractive for a wide range of applications,³ such as energy storage devices,⁴ organic electronics,^{6,7} and sensors.^{8,9}

In particular, g-C₃N₄ has been extensively studied⁵ for photocatalytic applications including solar-driven hydrogen evolution,^{10,11} CO₂ reduction,¹² and organic pollutant degradation.^{13–19} In this framework, very recently, g-C₃N₄ has also been investigated for its potential use in photocatalytic nitrogen fixation, i.e. reduction of gaseous N₂ to ammonia (NH₃) operated by sunlight, one among the most arduous and rewarding task in the field of heterogeneous photocatalysis.^{20,21}

Although nitrogen fixation is challenging due to the high stability of the N-N triple bond, the layered structure of g-C₃N₄ and its nitrogen-rich framework make it amenable to defect engineering and heterojunction formation, which, in turn, enable its employment as photocatalyst for promoting N₂ activation. Nevertheless, its photocatalytic performance is limited by poor intrinsic conductivity, rapid charge-carrier recombination, and a low density of active sites for N₂ adsorption and reduction.^{22,23} In this context, strategies such as intrinsic defect engineering, heteroatom doping, and heterojunction formation, have proved to be effective in the modulation of the electronic structure, by introducing in-gap states which extends visible-light absorption, enhance charge separation, and ultimately improve photocatalytic efficiency.^{2,3,13–19,24–28}

^a Dipartimento di Chimica e Biologia Adolfo Zambelli, Università di Salerno, Via Giovanni Paolo II, I-84084 Fisciano (SA), Italy. E-mail: alelandi1@unisa.it

^b Dipartimento di Scienze, Università degli Studi della Basilicata, Viale dell'Ateneo Lucano, 10 - 85100 Potenza, Italy. E-mail: francesco.ambrosio@unibas.it

^c Energy and Materials Chemistry Group, Department of Chemistry and INSTM, University of Pavia, Via Taramelli 16, Pavia, 27100, Italy.

^d Department of Chemistry, University of Pavia, Via Taramelli 16, Pavia, 27100, Italy

^e Department of Physics, Chalmers University of Technology, SE-412 96 Gothenburg, Sweden.

[†] Electronic Supplementary Information (ESI) available: Computational details of the DFT methodology and charge transition levels calculations; validation of the hybrid functional and robustness of defect charge-transition levels; structural, energetic, and statistical analyses of buckling in pristine and defective g-C₃N₄; spin-state energetics, optimized geometries, and SOMO isodensity plots for different supercells containing neutral nitrogen vacancies; details about electrostatic finite-size corrections for charged defects; and the relative stability and spin configurations of charged central and edge nitrogen vacancies., See DOI: 00.0000/00000000.



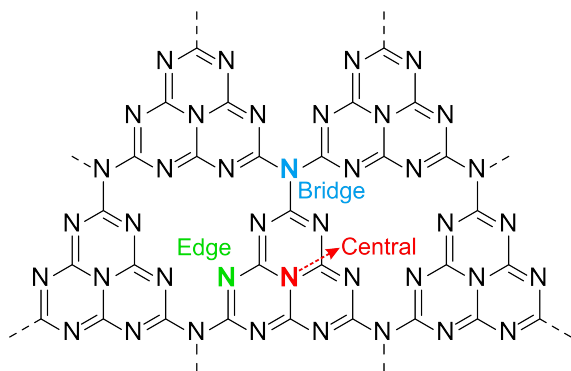


Fig. 1 Pictorial representation of the $P6/m2$ heptazine-based network, highlighting, by color code, the nitrogen sites where vacancies can occur.

Among intrinsic defects, nitrogen vacancies (V_N) have received particular attention: various methods have been developed to control their concentration in the sample, either using precursors yielding vacancy-rich structures^{29,30} or via post-synthesis thermal treatments.³¹ From a microscopic perspective, nitrogen vacancies are not all chemically equivalent, as they can be formed in three distinct locations of the heptazine-based network, corresponding to removal of a neutral nitrogen atom (i) at the center of heptazine, $V_N^0(C)$, (ii) on the edge of the fused rings, $V_N^0(E)$, and (iii) bridging two units in the periodic 2D lattice $V_N^0(B)$, see Figure 1. These should be considered as different defects, possibly giving distinct chemical behavior and electronic signatures.^{31–33}

Since the nature of the probed defects at the atomistic level is beyond reach for experimental characterization, theoretical and computational efforts have been deployed to unveil the defect physics underlying the measured properties.^{2,16,31,34,35} However, current studies do not provide a microscopic physical picture always fully consistent with the experimental characterization. This could be related to several factors, such as employing relatively small supercells for the simulations, as it has been done in several works,^{31,35} often assuming an idealized, perfectly flat layer. However, in two-dimensional materials, corrugation is known to significantly affect the structural and electronic properties;^{36–38} such an effect may be extended over large distances, thus requiring sufficiently large supercells to be properly accounted for.³⁹ In particular, buckling in $g-C_3N_4$ is known to relieve electrostatic repulsion between lone pairs on adjacent nitrogen atoms, thereby stabilizing the structure.⁴⁰ Thus, a correct description of corrugation in $g-C_3N_4$ is essential for an accurate prediction of adiabatic and vertical charge-transition levels, together with defect reorganization energies, all features required to provide a reliable microscopic interpretation of the vast body of spectroscopic and photocatalytic studies conducted on N-deficient $g-C_3N_4$.^{3,31,32,41–49}

Motivated by these challenges, we here investigate the electronic structure of $g-C_3N_4$ containing N vacancies, using periodic supercell calculations based on advanced hybrid density functional theory (DFT). Our approach fully accounts for the effects of corrugation and its size-dependence, to achieve both convergence of electronic properties and a robust description of the defects energetics, enabling identification of the most stable moi-

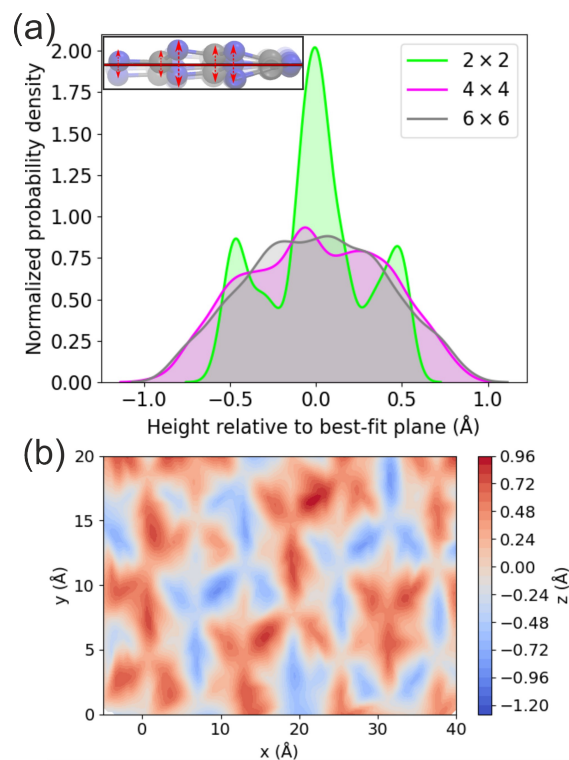


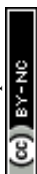
Fig. 2 (a) Comparison of the distribution of out-of-plane atomic distortions with respect to mean plane (see inset) for the three supercells under study. (b) Contour plot visualizing the atomic z -coordinate variations across the (x,y) plane in the 4×4 relaxed $g-C_3N_4$ structure. See also Figure S4 in the ESI.

eties. This framework allows us to connect the calculated properties with a plethora of experimental observations: first and most important (i) we rationalize the activity of N-deficient $g-C_3N_4$ towards photo-reduction and photo-oxidation in terms of the alignment between defect energy levels and relevant redox potentials. Moreover, we attribute (ii) experimental red-shifted absorption in N-deficient samples and (iii) the measured photoluminescence quenching to deep in-gap donor levels, arising from charge localization at the vacancy site.

To this end, we employ hybrid DFT including non-local electron correlation effects (see section S1, ESI) - a computational approach previously applied to a broad range of π -conjugated systems (including fullerenes, covalently bonded fullerene networks,⁵⁰ and acenes^{51,52}) - to investigate pristine and N-deficient monolayer $g-C_3N_4$.

As an initial model for the pristine material, we adopt the idealized flat $P6/m2$ heptazine-based network (Figure S1, ESI) proposed by Teter and Hemley⁵³, which is widely used as repeating unit for the fully condensed system.⁵⁴ Supercells of the 2D monolayer with increasing size are then constructed by replicating n times (where $n = 2, 4, 6$) the unit cell along the a and b directions. In the following, these supercells are denoted as 2×2 , 4×4 , and 6×6 , respectively. The latter comprises up to 1008 atoms (see Table S1 for details), a system size at the forefront of the current state of the art.

Structural relaxation of initially planar $g-C_3N_4$ monolayers in-



structure	planar			buckled			2×2 replicas		
	C	E	B	C	E	B	C	E	B
2×2	+0.79	0.00	+3.49	0.00	+0.54	+1.49	0.00	+0.03	+2.48
4×4	+0.80	0.00	+3.24	+0.57	0.00	+1.12	+0.02	0.00	+1.88
6×6	+1.01	0.00	+3.30	+0.60	0.00	+1.20	+0.01	0.00	+1.81

Table 1 Relative energy (in eV) for V_N^0 in central (C), edge (E) and bridge (B) position, as calculated for different supercell sizes of g- C_3N_4 monolayer models and considering ideal planar, fully relaxed (buckled) and replicas of 2×2 buckling structural configurations (vide infra). For each entry, the most stable defect is highlighted in red font.

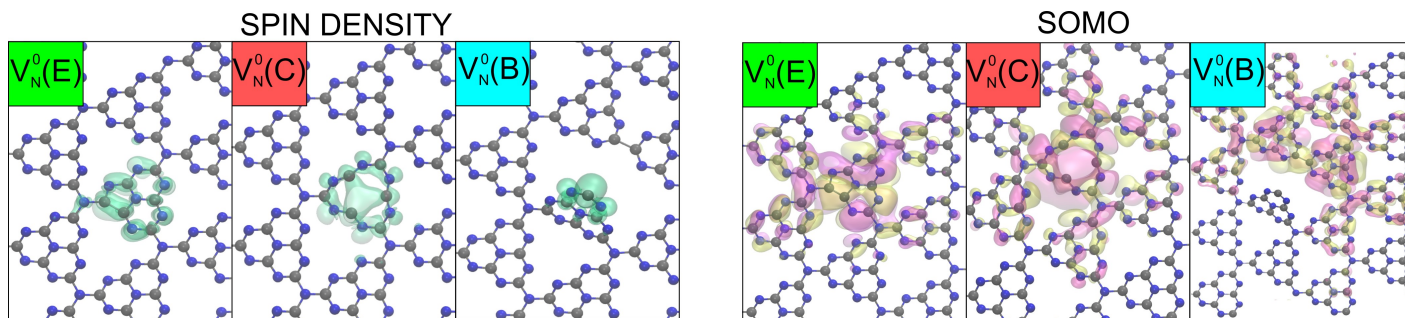


Fig. 3 Stick&ball top-view representation of the 4×4 g- C_3N_4 monolayer bearing a neutral N vacancy in different positions: central (left panel), edge (middle panel) and bridge (right panel). C and N atoms are colored in grey and blue, respectively. The isodensity representations of the spin density are given in green (isovalue 0.001 a.u.) in the left three panels, while isodensity representations of the singly-occupied molecular orbitals (SOMO) is illustrated in magenta and yellow in the three panels on the right.

variably leads to buckled configurations, irrespective of supercell size, accompanied by a substantial lowering of the total energy relative to the planar geometry (Table S2, ESI). Although the Mermin–Wagner theorem predicts the instability of long-range planar order at finite temperature,^{55,56} the emergence of buckling already at the DFT level (0 K) can be rationalized by partial relief of angular strain in N-containing bonds and a reduction of lone-pair repulsion.^{38,57,58} Analysis of the relaxed structures reveals a pronounced supercell-size dependence of the out-of-plane distortions. The 2×2 supercell exhibits only modest corrugation, with a mean absolute height ($MAH = \frac{1}{N} \sum_i |h_i|$, h_i being the signed distance of each atom i from the plane, see ESI) of 0.23 Å, a largest buckling amplitude ($LBA = \max_i(h_i) - \min_i(h_i)$) of 1.08 Å (see ESI for details), and a narrow distribution of atomic displacements (Figure 2a). In contrast, the 4×4 and 6×6 supercells display significantly larger and broadly distributed distortions, with $MAH = 0.33$ Å and $LBA = 1.79$ Å (Figure 2a). Contour plots of the atomic z coordinates across the (x, y) plane further reveal a periodic buckling pattern, indicative of a delocalized and ordered corrugation rather than isolated protrusions (Figure 2b). In the ESI (Fig. S4), we report the same contour plot with the projected atomic positions overlaid to clarify which atoms are associated with out-of-plane distortions. Comparison of different supercells (Figures S3–S4) shows that the 2×2 cell cannot fully accommodate the long-range nature of the buckling, as evidenced by its altered corrugation periodicity, while the 4×4 supercell emerges as the minimal size required to achieve reasonably converged structural properties.

Next, we move onto the characterization of the neutral N vacancy, V_N^0 , considering its possible different positions, see Figure 1. To evaluate how buckling affects the defect energy, we consider

removal of one N from 2×2 , 4×4 , and 6×6 supercell. Then, for each defect in each supercell, we perform structural relaxations in three different ways: either (i) enforcing the initial planarity of the 2D system by constraining the position of the nuclei on the z axis; (ii) fully relaxing the supercell, leading to buckled structures (much more stable than planar configurations, Table S2, ESI); and (iii) building 4×4 and 6×6 models as replicas of the corrugated pristine 2×2 supercell.

In this latter case, the 2×2 buckling is preserved by fixing the z coordinate during relaxation after removing one nitrogen atom to create the vacancy. This system is used to separate the effects on the total energy arising from different corrugation in different supercells, from that of local defect relaxation, and from possible electrostatic finite-size effects due to excitonic charge localization at the defect.⁵⁹

For each model, we compare the relative stability of $V_N^0(C)$, $V_N^0(E)$, and $V_N^0(B)$. The results are collected in Table 1 and refer to the doublet spin state of V_N^0 , which is always found to be lower in energy by more than 1.5 eV, with respect to quartet state (Table S3, ESI).

Inspection of Table 1 immediately reveals that $V_N^0(B)$ is consistently the least stable defect. This instability arises from the substantial structural reorganization induced by this vacancy, which involves significant distortion of the dangling heptazine units; notably, one unit tilts almost perpendicular to the plane of the material layer, see Figure 3. Such a pronounced relaxation comes at a high elastic cost, thus explaining the poor stability of this defect with respect to the other ones for all the considered systems, particularly when planarity is forced. Therefore, in the following discussion, we focus mainly on the competition between $V_N^0(C)$ and $V_N^0(E)$.



Our results indicate that the relative stability of these latter two defects is highly dependent on the local structure around the N vacancy. This, in turn, is connected with the degree of buckling allowed by the supercell size. First, the results obtained for the constrained planar structures show that the edge defect is by far the most stable, with energy differences up to 1 eV with respect to the central vacancy, see Table 1. Conversely, when considering the buckled structures, $V_N^0(C)$ is found to be the most stable N vacancy in the 2×2 supercell, see Table 1. However, we observe a remarkable inversion in relative stability when moving to the 4×4 supercell: the total energy of $V_N^0(E)$ is found to be 0.57 eV lower than that of $V_N^0(C)$. This trend appears to be fairly converged for the 6×6 supercell. Finally, $V_N^0(C)$ and $V_N^0(E)$ become almost iso-energetic in both 4×4 and 6×6 supercells, when keeping the corrugation fixed to that of the pristine 2×2 cell, thus highlighting the importance of local structural relaxations in conjunction with global corrugation of the material. Taken together, the results achieved for different models clearly indicate that (i) out-of-plan distortions, both locally induced by the defect and naturally ensuing from pristine $g\text{-C}_3\text{N}_4$, determine the relative stability of different defects and (ii) the reduced corrugation available for small supercells may lead to an incorrect evaluation of the defects relative stability.

By inspecting the local structure of the different defects in the buckled supercells, we observe that the removal of the central N atom in $V_N^0(C)$ yields to the formation of a 5-membered ring fused with a larger 9-membered ring for the 2×2 cell (Figure S6, ESI), while an extended ring involving the whole heptazine unit is found for both 4×4 (Figure 3) and 6×6 systems, thus further proving how a small supercell may provide incorrect local structures. In contrast, $V_N^0(E)$, for any supercell size, is always found to feature reorganization of the local bonding into a small 5-membered ring upon formation of a bond between the dangling C atoms, adjacent to the vacancy, see Figure 3. This ring, comprising two carbon and two nitrogen atoms together with the C–C bond formed at the defect site, is topologically analogous to an imidazole-type heterocycle, and its formation reflects the tendency of the unsaturated carbon centers to recover a locally aromatic coordination environment.

The introduction of nitrogen vacancies leads to a reduction in the degree of buckling of the $g\text{-C}_3\text{N}_4$ layer. In particular, for the central defect, the two-dimensional height map (Figure S5) reveals that the characteristic periodic distortions observed in the pristine structure are largely suppressed near the defect site, giving rise to a more planar morphology. This flattening effect suggests that the removal of a nitrogen atom locally relieves internal strain, leading to an extended ring structure that is more stabilized in absence of long-range out-of-plane distortions. Conversely, for the external defect, $V_N^0(E)$, this effect is lower as the replacement of one 6-atoms ring with a 5-atoms ring has a reduced impact on the global structure of $g\text{-C}_3\text{N}_4$. Therefore, $V_N^0(E)$, with its more compact structure, better fits inside the natural distortions of the two-dimensional network, see Figure S5, thus justifying its greater stability.

We next focus on the electronic properties, calculated for the 4×4 supercell, which showed fairly converged structure and en-

ergetics. First, from inspection of the spin density as well as from the frontier orbitals (Figure 3 and S6-S7), we observe that (i) all the three types of vacancies show spin localization on the defective heptazine unit (ii) $V_N^0(C)$ and $V_N^0(E)$ also present a localized Kohn-Sham energy level in the band gap of the material (see also Figure S2 in the ESI). Therefore, from an electronic-structure perspective, all three defects could be in principle related with the observed EPR spectra.⁶⁰ However, only $V_N^0(C)$ and $V_N^0(E)$ may provide the charge localization which can be responsible for boosting photocatalytic activity of $g\text{-C}_3\text{N}_4$ samples.⁶¹ Therefore, in the following, we focus on the electronic structure and the energy levels associated only with $V_N^0(E)$ and $V_N^0(C)$. It is important to mention that, although the calculated energetics would suggest dismissing the central vacancy as a relevant defect in isolated $g\text{-C}_3\text{N}_4$, the extent of buckling may depend on interactions between $g\text{-C}_3\text{N}_4$ and an underlying substrate when forming a heterojunction. Such interfacial interactions in experimentally realized heterostructures or chemically modified samples could, in principle, alter the corrugation pattern and thereby modify the relative defect stability.

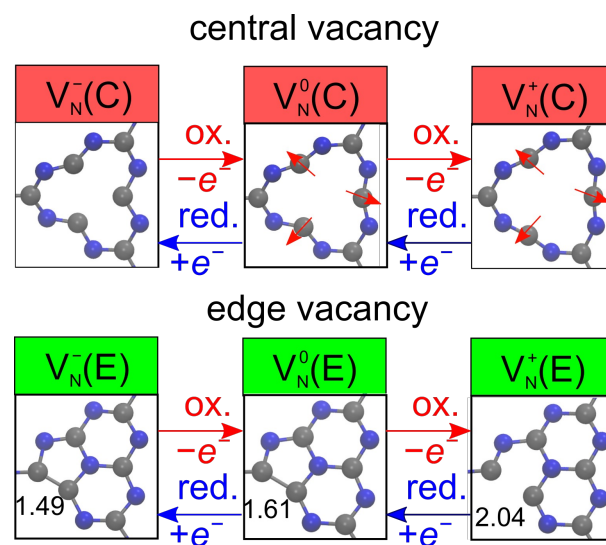


Fig. 4 Stick&ball representation of the local structure for central and edge N vacancies in monolayer $g\text{-C}_3\text{N}_4$ at varying charge states. Red arrows in top panels indicate the breathing motion of the 12-atoms ring of the central defect, while in the bottom panels we report the variation of the relevant C-C distance (in Å) for the edge defect.

Starting from the neutral defects, we next determine whether they can accept and/or donate electrons. To this end, we consider both positively and negatively charged vacancies, V_N^+ and V_N^- , respectively, for central and edge defects. For $V_N(C)$, we observe sizable reconstruction of the 9-membered ring, upon oxidation/reduction, see Figure 4. In particular, injection of an electron brings to a tightening of the honeycomb-like structure, closer to that of the original pristine heptazine unit. At variance with this, electron detachment is found to further enhance the reconstruction of the 9-atoms ring, observed for the neutral defect, towards a swollen and rounder moiety. For $V_N(E)$, on the other hand, the reorganization of the edge defect upon variation of charge state is much more localized, involving mainly the C-C bond observed



for the neutral system, Figure 4. This bond is found to be shortened from 1.61 to 1.49 Å, upon reduction, while it breaks in the oxidized defect.

Spin-polarized calculations show that singlet configurations are strongly favored over triplets, by ≈ 1 eV in the +1 state and ≈ 0.6 eV in the -1 state, see Table S3. These large singlet-triplet splittings preclude thermal population of triplet states. These results are still compatible with experimental reports of triplet involvement inferred under photo-excitation, which must originate from non-equilibrium excited-state processes.⁶² It is also worth noting that, while the relative stability of $V_N(C)$ and $V_N(E)$ defects estimated for the neutral vacancy is preserved for the reduced species, an opposite trend is observed for the oxidized defect, for which the $V_N(C)$ structure is found to be favored by as much as 0.35 eV (Table S4). However, under typical synthesis conditions, g-C₃N₄ is intrinsically *n*-type, favoring neutral or negatively charged nitrogen vacancies.⁶³ The positively charged central vacancy would become thermodynamically favorable only under strongly *p*-type conditions, which are not commonly realized in as-grown materials.²⁸ The possibility of $V_N^+(E) \rightarrow V_N^+(C)$ interconversion upon photo-excitation should also be ruled out as a sizable barrier is expected for the migration of a tri-coordinated N atom. This implies that, once formed, each defect configuration is indeed kinetically frozen.

We now turn to the calculation of the charge transition levels (CTL) associated with the investigated nitrogen vacancies, employing the grand-canonical formalism for defects in crystalline semiconductors^{64–66} (see Section S2 of the ESI). The resulting values, reported in Table 2 and Figures 5–6, define the thermodynamic stability of the different charge states and provide the basis for interpreting the photocatalytic and spectroscopic behavior of defective g-C₃N₄.

Impact on photocatalysis. The $V_N^0(C)$ and $V_N^0(E)$ defects feature (0/−) CTL at 2.63 and 2.59 eV above the valence band maximum (VBM), respectively. Considering the calculated and experimental gap of 2.7 eV¹⁷, these are shallow acceptor levels at ≈ 0.1 eV below the conduction band minimum (CBM) of g-C₃N₄ (see Figure 6). Such levels are consistent with the improved visible absorption and moderate carrier trapping, observed for g-C₃N₄ samples with mild concentrations of N vacancies.^{31,32} At variance, the adiabatic (+/0) levels are found at 1.70 and 0.82 eV above the VBM of g-C₃N₄, for $V_N(C)$ and $V_N(E)$, respectively, both representing deep donor defects in the band gap.

To assess the implications for photocatalysis, in Figure 6 we also report the alignment of these adiabatic defect levels at the semiconductor-water interface, taking advantage of the band alignment from Ref. 17. The redox potential of reactions typically targeted by photocatalysis, i.e. H₂ production, N₂ fixation, and water oxidation are included for comparison. That alignment evidences that acceptor levels for both central and edge defects are favorably positioned against H⁺/H₂ and N₂/NH₃ potentials. This, coupled with the shallow trapping of electrons, is expected to promote electron transfer toward reduction reactions, thereby enhancing photo-reduction yields.

Conversely, holes trapped at the vacancy site are associated with deep donor levels that lie far above the H₂O/O₂ oxida-

tion potential, deteriorating the otherwise favorable alignment between the pristine VBM and the water oxidation level. The overall picture is in full agreement with the available experimental evidence that N-deficient g-C₃N₄ increases the yield of photo-reduction reactions but worsens performances towards photo-oxidation processes.^{42–49}

Interpretation of UV absorption spectra. We now analyze the vertical energy levels, to rationalize defect-mediated UV-Vis transitions. As shown in the configurational coordinate diagrams (Figure 5) two excitation channels can be considered: (i) for acceptor-like defects, we consider excitation of an electron from the valence band of g-C₃N₄ to the defect level, VBM \rightarrow (0/−) CTL. Conversely, for donor-like defects, we consider excitation from the defect level to the conduction band: (0/+) \rightarrow CBM.

The VBM \rightarrow (0/−) vertical transition fall at ΔE of 3.3 eV and 2.8 eV for the central and edge defects, respectively, very close to the experimental gap of pristine g-C₃N₄ (2.7–2.9 eV^{4,5}). Thus, that transition does not introduce a significantly lower-energy absorption channel and cannot account for the experimentally observed reduction of the optical gap (2.0–2.5 eV)^{31,32,41} in defective samples. In contrast, vertical excitation of an electron from the oxidized defect (0/+) to the CBM (after inclusion of excitonic effects, which decrease the gap by 0.32 eV, cf. ESI) yields ΔE of 1.73 eV for the central defect and 2.09 eV for the edge defect, this latter in excellent agreement with the gap of defective g-C₃N₄.

In other words, among the four charge-transition levels considered, only the (+/0) \rightarrow CBM transition associated with the edge vacancy remains consistent with the experimentally observed absorption range for defective samples e g-C₃N₄; therefore, we conclude that (i) the spectroscopic signatures of N vacancies in g-C₃N₄ originate from donor-type transitions, and (ii) these experimental absorption features can be attributed to the edge vacancy $V_N(E)$, thus corroborating our previous analysis of defect energetics.

Photoluminescence quenching. Finally, both vertical and adiabatic quantities provides insight into the experimentally observed photoluminescence quenching in N-deficient carbon nitride.^{31,32,41} First of all, as discussed above, donor levels are located deep into the band gap, possibly enhancing non-radiative recombination channels and thus reducing photoluminescence.^{31,32,41}

Furthermore, for all considered defects, the peak energies of the optical transitions differ markedly from the corresponding adiabatic charge transition levels (Table 2 and Figure 5). This difference originates from the pronounced structural relaxation upon oxidation or reduction (Figure 4), which results in sizable reorganization energies (Table 2). The effect is particularly pronounced for the (+/0) transition, where $\lambda_{q \rightarrow q'}$ reaches 1.05 eV for the central defect, but in general, except for the reduction of the edge defect where the λ is comparatively small (0.21 eV), all charge-state changes involve substantial lattice rearrangements. The resulting wide separation of the potential-energy surfaces favors non-radiative multi-phonon relaxation over radiative recombination, providing a natural explanation for the experimentally reported photoluminescence quenching in N-deficient g-C₃N₄.^{31,32,41} In this regard, we note that reorganization energies



defect position	μ^{ad}		$\mu_{q \rightarrow q'}^{\text{opt}}$				$\lambda_{q \rightarrow q'}$			
	(0/-)	(+/0)	0 \rightarrow -	- \rightarrow 0	0 \rightarrow +	+ \rightarrow 0	0 \rightarrow -	- \rightarrow 0	0 \rightarrow +	+ \rightarrow 0
central	2.63	1.70	3.33	2.20	0.65	2.32	0.70	0.43	1.05	0.62
edge	2.59	0.82	2.80	1.87	0.29	1.51	0.21	0.62	0.53	0.69

Table 2 Calculated adiabatic (μ^{ad}) and optical vertical ($\mu_{q \rightarrow q'}^{\text{opt}}$) CTL for central and edge V_{N} defects, along with corresponding reorganization energies, $\lambda_{q \rightarrow q'}$. q and q' denote the initial and final charge states. Adiabatic CTLs refer to fully relaxed initial and final geometries, whereas vertical CTLs are evaluated at fixed geometry (see ESI). All values are given in eV relative to the VBM (set to 0 eV).

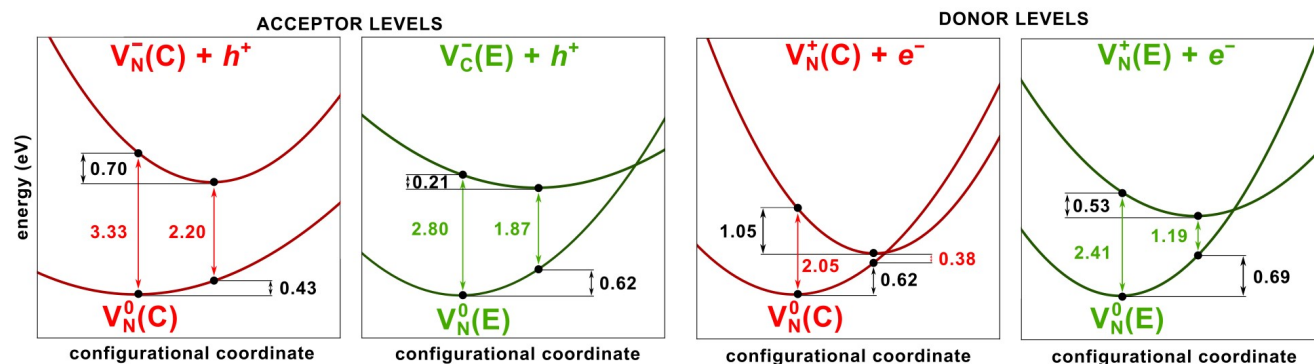


Fig. 5 Calculated configuration coordinate diagrams for central and edge N vacancies in $g\text{-C}_3\text{N}_4$. The two left panels refer to recombination of a hole with the reduced defect (via acceptor levels), while the two right panels to recombination of an electron with the oxidized vacancy (via donor levels).

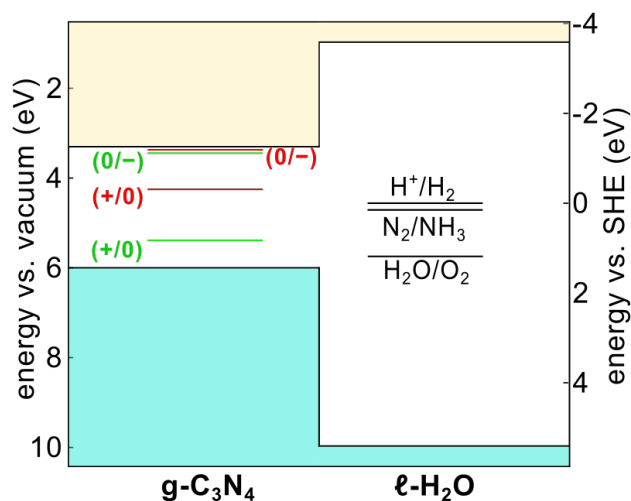


Fig. 6 VBM and CBM of $g\text{-C}_3\text{N}_4$ aligned with (i) the band edges of liquid water ($l\text{-H}_2\text{O}$) and (ii) the redox levels associated with aqueous proton reduction, nitrogen fixation, and water oxidation. Energies are reported relative both to the vacuum level and the computational standard hydrogen electrode (SHE) of Refs. 67,68. The VBM and CBM of $g\text{-C}_3\text{N}_4$ lie 6.00 and 3.30 eV below the vacuum level, respectively.¹⁷ The corresponding band-edge positions of liquid water (9.97 and 0.97 eV vs. vacuum) are taken from Ref. 68. Adiabatic charge transition levels of defects (0/+) and (0/-) in the band gap of $g\text{-C}_3\text{N}_4$ are aligned to the VBM of $g\text{-C}_3\text{N}_4$ as reported in Table 2; red and green lines correspond to $V_{\text{N}}(\text{C})$ and $V_{\text{N}}(\text{E})$ vacancies, respectively.

below 0.1 eV are calculated for the relaxation of charge carriers in the pristine material, as a consequence of a larger delocalization of both holes and electrons, cf. Figure S10 and Section S8 of the ESI. Therefore, we predict a small difference between the vertical and adiabatic band gap of pristine $g\text{-C}_3\text{N}_4$, which is consistent with the red shifts below 0.1-0.2 eV observed in emission spec-

tra and the small separation between potential energy surfaces agrees with the absence of PL quenching in pristine samples.¹⁷

In conclusion, we carried out a systematic ab-initio study establishing a comprehensive framework for understanding nitrogen vacancies in $g\text{-C}_3\text{N}_4$. By performing advanced DFT calculations on systems exceeding a thousand atoms, we showed that convergence of long-range buckling is essential for correctly predicting both the relative stability and electronic properties of defects, as small supercells fail to capture the collective out-of-plane distortions that stabilize pristine and defective systems, an effect often overlooked in prior studies. Calculated adiabatic and optical charge transition levels enable direct comparison with experiments, reproducing the red-shifted absorption (2.0–2.5 eV) and connecting large reorganization energies (up to 1.05 eV) with photoluminescence quenching and shortened emission lifetimes in N-deficient samples. Most importantly, band alignment at the semiconductor-water interface rationalizes the observed enhancement of photo-reduction reactions alongside deteriorated photo-oxidation performance, linking defect energetics to catalytic selectivity. To our knowledge, this is the first theoretical study to comprehensively correlate calculated defect properties of $g\text{-C}_3\text{N}_4$ with multiple important experimental observables, such as absorption spectra, photoluminescence behavior, and photocatalytic efficiency. By connecting atomic-scale defect structure with macroscopic performance, our work provides a predictive framework protocol for rational design of defect-engineered $g\text{-C}_3\text{N}_4$ with tailored optoelectronic and catalytic properties. Furthermore, our computational methodology can be extended both to (i) other defect types (carbon vacancies, dopants) and (ii) related two-dimensional carbon nitride materials, making it a general and transferable tool for predictive modeling and targeted



optimization of (metal-free) photocatalysts.

Data availability

The data supporting this article have been included as part of the ESI.

Conflicts of interest

There are no conflicts to declare.

Acknowledgements

A.L. acknowledges PRIN 2022 grant 2022XSC9P5 (INTESA-SOLE) by Ministero di Università e Ricerca (MIUR) and FARB 2025 grant from Università di Salerno for funding. F.A. and M.L. acknowledge PRIN 2022-PNRR grant (P2022W9773) for funding. A.L., F.A. and M.L. acknowledge the CINECA award under the ISCRa initiative, for high-performance computing resources: projects MHP-DEF and Photofix. J.W. acknowledges funding from the Swedish Strategic Research Foundation through a Future Research Leader programme (FFL21-0129), the Swedish Research Council (2019-03993), European Research Council (ERC Starting Grant no. 101162195), and the Knut and Alice Wallenberg Foundation (2023.0032 and 2024.0042). A.P. acknowledges PRIN 2022 grant 2022TWKM4X.

Conflicts of interest

There are no conflicts to declare.

References

- G. O. Hartley and N. Martsinovich, *Faraday Discuss.*, 2021, **227**, 341–358.
- M. Chen, M. Sun, X. Cao, H. Wang, L. Xia, W. Jiang, M. Huang, L. He, X. Zhao and Y. Zhou, *Coord. Chem. Rev.*, 2024, **510**, 215849.
- J. Lin, W. Tian, H. Zhang, H. Sun and S. Wang, *Acc. Chem. Res.*, 2024, **57**, 2303–2315.
- M. Subbiah, A. Mariappan, A. Sundaramurthy, S. Venkatachalam, R. T. Renganathan, N. Saravanan, S. Pitchaimuthu and N. Srinivasan, *ACS Omega*, 2024, **9**, 11273–11287.
- N. T. T. Ha, P. T. Be, P. T. Lan, N. T. Mo, L. M. Cam and N. N. Ha, *RSC Adv.*, 2021, **11**, 16351–16358.
- H. Y. Hoh, Y. Zhang, Y. L. Zhong and Q. Bao, *Adv. Opt. Mater.*, 2021, **9**, 2100146.
- J. Bian, C. Huang and R. Zhang, *ChemSusChem*, 2016, **9**, 2723–2735.
- R. Malik, N. Joshi and V. K. Tomer, *Coord. Chem. Rev.*, 2022, **466**, 214611.
- L. Chen and J. Song, *Adv. Funct. Mater.*, 2017, **27**, year.
- R.-H. Gao, Q. Ge, N. Jiang, H. Cong, M. Liu and Y.-Q. Zhang, *Frontiers in Chemistry*, 2022, **10**, year.
- S. Yang, Y. Gong, J. Zhang, L. Zhan, L. Ma, Z. Fang, R. Vajtai, X. Wang and P. M. Ajayan, *Adv. Mater.*, 2013, **25**, 2452–2456.
- S. Bhowmik, S. J. Phukan, N. K. Sah, M. Roy, S. Garai and P. K. Iyer, *ACS Applied Nano Materials*, 2021, **4**, 12845–12890.
- M. Corti, R. Chiara, L. Romani, B. Mannucci, L. Malavasi and P. Quadrelli, *Catal. Sci. Technol.*, 2021, **11**, 2292–2298.
- M. Medina-Llamas, A. Speltini, A. Profumo, F. Panzarea, A. Milella, F. Fracassi, A. Listorti and L. Malavasi, *Nanomaterials*, 2023, **13**, 263.
- J. Pei, H. Li, D. Yu and D. Zhang, *Catalysts*, 2024, **14**, 825.
- C. Tedesco, L. Gregori, A. Simbula, F. Pitzalis, A. Speltini, F. Merlo, S. Colella, A. Listorti, E. Mosconi, A. A. Althman, W. Kaiser, M. Saba, A. Profumo, F. De Angelis and L. Malavasi, *Adv. Energy Sustainability Res.*, 2024, **5**, 2400040.
- L. Romani, A. Speltini, C. N. Dibenedetto, A. Listorti, F. Ambrosio, E. Mosconi, A. Simbula, M. Saba, A. Profumo, P. Quadrelli, F. De Angelis and L. Malavasi, *Adv. Funct. Mater.*, 2021, **31**, 2104428.
- Y. Baghdadi, F. Temerov, J. Cui, M. Daboczi, E. Rattner, M. S. Sena, I. Itskou and S. Eslava, *Chem. Mater.*, 2023, **35**, 8607–8620.
- Y. Baghdadi, M. Daboczi, F. Temerov, M. Yang, J. Cui and S. Eslava, *J. Mater. Chem. A*, 2024, **12**, 16383–16395.
- R. Huang, X. Li, W. Gao, X. Zhang, S. Liang and M. Luo, *RSC advances*, 2021, **11**, 14844–14861.
- X.-C. Tang, Z. Ding, Z.-H. Wang, N. Arif, Y.-Y. Chen, L. Li and Y.-J. Zeng, *ChemCatChem*, 2024, **16**, e202401355.
- Z. Zhang, S. Hou, T. Wang, S. Liu, X. Gao, C. Wang and G. Wang, *Small*, 2022, **18**, year.

- G. Dong, W. Ho and C. Wang, *J. Mater. Chem. A*, 2015, **3**, 23435–23441.
- Y. Zhang, T. Mori, J. Ye and M. Antonietti, *J. Am. Chem. Soc.*, 2010, **132**, 6294–6295.
- P. Niu, G. Liu and H.-M. Cheng, *J. Phys. Chem. C*, 2012, **116**, 11013–11018.
- J. Fu, J. Yu, C. Jiang and B. Cheng, *Adv. Energy Mater.*, 2018, **8**, 1701503.
- A. Bafekry, M. Faraji, N. Hieu, A. Bagheri Khatibani, M. M. Fadlallah, D. Gogova and M. Ghergherehchi, *Appl. Surf. Sci.*, 2022, **583**, 152270.
- Y. Zhang, P. Lian, X. Hao, L. Zhang, L. Yang, L. Jiang, K. Zhang, L. Liao and A. Qin, *Inorganics*, 2025, **13**, 225.
- H. Yu, R. Shi, Y. Zhao, T. Bian, Y. Zhao, C. Zhou, G. I. N. Waterhouse, L. Wu, C. Tung and T. Zhang, *Adv. Mater.*, 2017, **29**, year.
- H. Chen, W. Wang, Z. Yang, X. Suo, Z. Lu, W. Xiao and S. Dai, *J. Mater. Chem. A*, 2021, **9**, 4700–4706.
- W. Tu, Y. Xu, J. Wang, B. Zhang, T. Zhou, S. Yin, S. Wu, C. Li, Y. Huang, Y. Zhou, Z. Zou, J. Robertson, M. Kraft and R. Xu, *ACS Sustainable Chem. Eng.*, 2017, **5**, 7260–7268.
- W. Xing, K. Cheng, Y. Zhang, J. Ran and G. Wu, *Nanomaterials*, 2021, **11**, 1480.
- F. Lin, T. Wang, Z. Ren, X. Cai, Y. Wang, J. Chen, J. Wang, S. Zang, F. Mao and L. Lv, *J. Colloid Interface Sci.*, 2023, **636**, 223–229.
- X. Liu, W. Kang, W. Zeng, Y. Zhang, L. Qi, F. Ling, L. Fang, Q. Chen and M. Zhou, *Appl. Surf. Sci.*, 2020, **499**, 143994.
- H. Chai, W. Chen, Z. Feng, Y. Li, M. Zhao, J. Shi, Y. Tang and X. Dai, *Nanomaterials*, 2023, **13**, 1433.
- A. Martín-Reicio, C. Romero-Muñiz, A. J. Martínez-Galera, P. Pou, R. Pérez and J. M. Gómez-Rodríguez, *Nanoscale*, 2015, **7**, 11300–11309.
- R. Singh, D. Scheinecker, U. Ludacka and J. Kotakoski, *Nanomaterials*, 2022, **12**, 3562.
- M. M. Mridha, S. Kellici and J. Buckeridge, *J. Phys. Chem. C*, 2025, **129**, 15109–15121.
- S. K. Jain, G. T. Barkema, N. Mousseau, C.-M. Fang and M. A. van Huis, *J. Phys. Chem. C*, 2015, **119**, 9646–9655.
- L. M. Azofra, D. R. MacFarlane and C. Sun, *Phys. Chem. Chem. Phys.*, 2016, **18**, 18507–18514.
- S. Hou, X. Gao, X. Lv, Y. Zhao, X. Yin, Y. Liu, J. Fang, X. Yu, X. Ma, T. Ma et al., *Nano-Micro Letters*, 2024, **16**, 70.
- H. Zhai, P. Tan, L. Lu, H. Liu, Y. Liu and J. Pan, *Catal. Sci. Technol.*, 2021, **11**, 3914–3924.
- Y. Li, M. Ti, D. Zhao, Y. Zhang, L. Wu and Y. He, *Journal of Alloys and Compounds*, 2021, **870**, 159298.
- J.-Y. Tang, X. Y. Kong, B.-J. Ng, Y.-H. Chew, A. R. Mohamed and S.-P. Chai, *Catal. Sci. Technol.*, 2019, **9**, 2335–2343.
- Y. Huang, T. Ding, W. Zuo, Z. Nie, M. Zheng and Y. Zeng, *Environmental Research*, 2025, **274**, 121302.
- G. Dong, W. Ho and C. Wang, *Journal of Materials Chemistry A*, 2015, **3**, 23435–23441.
- H. Shang, X. Ye, H. Jia, Q. Zhu, D. Zhang, D. Wang and G. Li, *Advanced Materials Technologies*, 2023, **8**, 2201579.
- L. Hou, X. Cui, B. Guan, S. Wang, R. Li, Y. Liu, D. Zhu and J. Zheng, *Nature*, 2022, **606**, 507–510.
- Q. Zhu and J. Zhang, *Environmental Functional Materials*, 2022, **1**, 121–125.
- A. Capobianco, J. Wiktor, A. Landi, F. Ambrosio and A. Peluso, *Nano Letters*, 2024, **24**, 8335–8342.
- A. Landi, F. Ambrosio, A. Leo, D. Padula, G. Prampolini and A. Peluso, *J. Mater. Chem. C*, 2025, **13**, 23855–23869.
- F. Ambrosio, J. Wiktor, A. Landi and A. Peluso, *J. Phys. Chem. Lett.*, 2023, **14**, 3343–3351.
- D. M. Teter and R. J. Hemley, *Science*, 1996, **271**, 53–55.
- E. Kroke and M. Schwarz, *Coord. Chem. Rev.*, 2004, **248**, 493–532.
- P. C. Hohenberg, *Phys. Rev.*, 1967, **158**, 383.
- N. D. Mermin and H. Wagner, *Phys. Rev. Lett.*, 1966, **17**, 1133.
- A. S. Ivanov, E. Miller, A. I. Boldyrev, Y. Kameoka, T. Sato and K. Tanaka, *J. Phys. Chem. C*, 2015, **119**, 12008–12015.
- J. Wang, D. Hao, J. Ye and N. Umezawa, *Chem. Mater.*, 2017, **29**, 2694–2707.
- T. Möslinger, N. Österbacka and J. Wiktor, *J. Phys. Chem. Lett.*, 2025, **16**, 6861–6865.
- X. Bi, L.-Z. Wang, D.-H. Zhai, L. Wang, H. Yang and G.-H. Du, *Sci. Rep.*, 2025, **15**, year.
- F. Ambrosio and J. Wiktor, *Appl. Phys. Lett.*, 2025, **126**, year.
- A. Actis, M. Melchionna, G. Filippini, P. Fornasiero, M. Prato, M. Chiesa and E. Salvadori, *Angew. Chem. Int. Ed.*, 2023, **62**, e202313540.
- X. Bi, L.-Z. Wang, D.-H. Zhai, L. Wang, H. Yang and G.-H. Du, *Scientific Reports*, 2025, **15**, 19864.
- C. Freysoldt, J. Neugebauer and C. G. Van de Walle, *Phys. Rev. Lett.*, 2009, **102**, 016402.
- H.-P. Komsa, T. T. Rantala and A. Pasquarello, *Phys. Rev. B*, 2012, **86**, 045112.
- M. Lorisio, S. Azmat, A. Listorti, A. Landi, J. Wiktor, F. De Angelis, A. Peluso, S. Colella and F. Ambrosio, *J. Phys. Energy*, 2025, **8**, 015009.
- F. Ambrosio, G. Miceli and A. Pasquarello, *J. Chem. Phys.*, 2015, **143**, 244508.
- F. Ambrosio, W. Chen and A. Pasquarello, *Phys. Chem. Chem. Phys.*, 2025, **27**, 23079–23090.

